RSC Advances

PAPER

View Article Online
View Journal | View Issue

Cite this: *RSC Adv.*, 2023, **13**, 11415

Mechanical alloying of $Mg_{0.8-X}Ti_{0.2}$ and study the effect of adding (x = 0.2 wt%) transition metal like Sc, Zr, or Nb on their phase transitions, activation energy, and hydrogen storage properties

K. S. Nivedhitha, †*[a] R. Venkatesh, †[a] N. R. Banapurmath, [b] T. M. Yunus Khan,[c] Chandramouli Vadlamudi,[d] Sanjay Krishnappa[d] and Sultan Alshehery[c]

Till now Mg-based alloys have attracted much attention due to the high storage capacity of hydrogen. An effort was made to evaluate the apparent activation energy and electrochemical behavior of transition metals such as scandium (Sc), zirconium (Zr), and niobium (Nb) alloyed with Mg–Ti. $Mg_{0.8}Ti_{0.2}$, $Mg_{0.6}Ti_{0.2}Sc_{0.2}$, $Mg_{0.6}Ti_{0.2}Zr_{0.2}$, and $Mg_{0.6}Ti_{0.2}Nb_{0.2}$ alloy powders were synthesized using high-energy ball milling. Ballmilled powders were subjected to structural and morphological characterization using X-ray diffraction and scanning electron microscopy respectively. A strong shift in the inter-planar spacing value of milled powders confirmed supersaturated solid solution of Ti and transition metals in Mg. The inter-planar spacing values before and after milling are found to be 0.24 and 0.21 nm, respectively. $Mg_{0.8}Ti_{0.2}$, $Mg_{0.6}Ti_{0.2}Sc_{0.2}$, and $Mg_{0.6}Ti_{0.2}Zr_{0.2}$ alloy powders result in the FCC phase while $Mg_{0.6}Ti_{0.2}Nb_{0.2}$ powders result in BCC phase, however, the entire powders have an amorphous background. SEM-EDS analysis of the milled powders confirmed the presence of Mg, Ti, Sc, Zr, and Nb elements with a small amount of oxygen. Selected area electron diffraction (SAED) pattern of $Mg_{0.8}Ti_{0.2}$ alloy powders exhibits a nanocrystalline nature owing to their polycrystalline ring pattern. Exothermic peak broadening increases after the substitution of Nb and Zr in $Mg_{0.8}Ti_{0.2}$ alloy powder, which exhibits a lower activation energy (188 kJ mol^{-1}) than others. In cyclic voltammetry, a drenched cathodic peak is observed for $Mg_{0.8}Ti_{0.2}$ at a potential around −0.83 V. In electrochemical impedance spectroscopy, the charge transfer resistance of $Mg_{0.6}Ti_{0.2}Sc_{0.2}$ is lower than that of $Mg_{0.6}Ti_{0.2}Zr_{0.2}$ and $Mg_{0.6}Ti_{0.2}Nb_{0.2}$ alloy but higher than $Mg_{0.8}Ti_{0.2}$ electrode materials, and charge–discharge studies were done on the developed electrode materials. It shows that $Mg_{0.8}Ti_{0.2}$ electrode material delivers a maximum discharge capacity of 535 mA h g^{-1}.

Received 16th November 2022
Accepted 23rd March 2023

DOI: 10.1039/d2ra07277g

rsc.li/rsc-advances

1. Introduction

The demand for energy and change in climatic conditions have motivated the scientific community to discover a novel material that can safely and efficiently carry and supply energy when needed.[1–5] Among various renewable and green energies, hydrogen is treated as a potential energy carrier. However, it is difficult to handle, store, and transport hydrogen for mobile applications. So, specific engineered materials may help to store hydrogen most safely. Here comes the role of materials-based research in tailoring suitable metals with appropriate synthesis routes to achieve superior microstructural changes for hydrogen storage applications.[6–10] Once the microstructure is tuned to meet the service conditions, safe and efficient handling of hydrogen for everyday use will follow automatically. The spectrum of hydrogen storage materials and their electrochemical characteristics are reported *viz.*, transition metal hydride, borohydrides, amides, binary, ternary, and complex metal hydrides.[11–14] Among them, hydrogen storage using transition metal hydride is the preferred choice of study owing to their unique electrochemical characteristics.[15–18] The A_2B_7 type Pr–Mg–Ni based alloy electrodes result in a maximum discharge capacity of 370 mA h g^{-1}, a high ex-change ion current density of 653 mA g^{-1}, and a high diffusion coefficient of 7.6 × 10^{-9} cm^2 s^{-1}.[19] The maximum discharge capacity of AB_5 type compound is 300 mA h g^{-1}.[20] Compared to AB_2, AB_5, and A_2B_7 alloys, nanostructured Mg–Ti alloys are extensively used in hydrogen storage applications. Possible reasons for employing Mg–Ti as a hydrogen-carrying medium

[a]*Centre of Excellence in Material Science, KLE Technological University, Hubballi, 580031, India. E-mail: k.s.nivedhitha@gmail.com*

[b]*School of Mechanical Engineering, Centre of Excellence in Material Science, KLE Technological University, Hubballi, 580031, India*

[c]*Department of Mechanical Engineering, College of Engineer King Khalid University, Abha, 616421, Saudi Arabia*

[d]*Aerosapien Technologies, Daytona Beach, Florida, USA*

† Both authors contributed equally to this manuscript.

could be due to its distinctive properties, such as low density, non-toxic, long-term stability, excellent thermodynamic stability, and low cost. Moreover, the fluorite structure of Mg–Ti alloy speeds up the hydrogen ion diffusion kinetics more than the rutile structure of pure MgH_2.[21,22] Incidentally, the presence of both octahedral and tetrahedral sites in Mg–Ti serves as a transport channel for the hydrogen atoms to occupy their respective vacant sites.[23] Also, the fabrication of Mg–Ti alloys using conventional routes is metallurgically limited due to a large gap in their melting points.

Unlike crystalline and amorphous Mg–Ti, it is difficult to synthesize and achieve nanostructures using traditional routes such as melt quenching, CVD, and PVD.[24–28] Constraints concerning melting point difference and the limited solid-solubility of Ti in Mg encouraged us to pick mechanical alloying (MA) as the appropriate method to synthesize nanostructured Mg–Ti alloys.[29] MA involves repeated or periodic trapping of powder particles between the colliding balls, leading to severe plastic deformation of powder particles. In this process, powder particles experience severe lattice distortions followed by fresh powder surface formation. Powder particles with fresh and reactive surfaces tend to enhance the hydrogen ion diffusion kinetics and activation behaviours too.[30] Apart from the nanocrystalline nature of Mg–Ti alloy, partial replacement of Mg with transition metals like Sc, Zr, and Nb is reported to have a significant effect on the electrochemical hydrogen storage characteristics. Sc exhibits lower density and higher reversible hydrogen storage capacity. It also rapidly changes its crystal structure from rutile to fluorite, which enhances the hydrogen ion mobility during the hydriding/dehydriding process.[31–35] The addition of Zr to the Mg–Ti alloy improves hydrogen ion diffusion kinetics and cyclic stability. A relatively bigger atomic radius of the Zr atom helps to create more vacant sites for storing hydrogen. In addition to it, Zr produces a thin oxide film over Mg–Ti alloy, which helps to increase the cyclic stability of the alloy powders.[36–42] Nb is known for its catalytic effect on the hydriding/dehydriding behaviour of Mg–Ti alloys.[43]

The present work is focused on the synthesis and structural characterization of transition metal alloys such as Sc, Zr, and Nb substituted Mg–Ti alloy. The apparent activation energy of milled powders is calculated by using Kissinger analysis and also study the effect of partial substitution of Sc, Zr, and Nb for Mg on the electrochemical hydrogen storage behaviour is discussed with supportive experimental evidence.

2. Materials and methods

2.1. Synthesis of $Mg_{0.8-x}Ti_{0.2}$ (X = Sc, Zr and Nb)

A planetary type ball milling instrument (In Smart Systems, Hyderabad, India) is used to prepare 0.2 wt% of Sc, Nb, and Zr substituted $Mg_{0.8-x}Ti_{0.2}$ intermetallic alloy powders. The milling instrument is programmed to work for 20 min forward rotation, 20 min rest, and 20 min reverse rotation in an hour. Elemental powders of Mg, Ti, Sc, Zr, and Nb 99% pure, purchased from Sigma Aldrich with a particle size of ~100 μm and purity of 99% were used to prepare metallic alloy powders. Powders were suitably weighed and transferred into stainless steel (SS) vials inside the glove box under high pure argon (99.99% pure) environment. Elemental powders were mechanically alloyed at room temperature using a high-energy planetary SS ball (10 mm in diameter) and a milling speed of 260 rpm under an argon atmosphere to avoid oxidation of the specimens. The weight ratio between ball and powder is set at 10 : 1, and the milling time is fixed for 30 hours. $Mg_{0.8}Ti_{0.2}$, $Mg_{0.6}Ti_{0.2}Sc_{0.2}$, $Mg_{0.6}Ti_{0.2}Zr_{0.2}$, and $Mg_{0.6}Ti_{0.2}Nb_{0.2}$ alloy powders were synthesized and subjected to further characterizations.

2.1.1. Structural characterization. Powder diffraction studies on the milled powders were carried out using a Rigaku Ultima III, X-ray diffractometer, Japan. The powder diffraction pattern was done with an accelerating voltage of 30 V and an acceleration current of 40 mA. The copper ($\lambda = 1.5418$ Å) target was used for X-ray generation. The X-ray pattern was recorded in the 2θ range of 30–70° with a scan rate of 0.02° s^{-1}. Phase evolution, crystallite size, and lattice strain of the milled powders were deduced from X-ray diffraction analysis. From the XRD pattern, the crystallites size estimated using Scherrer equation and macro-strain (%) was calculated by the simplified Williamson–Hall relationship using following equation

$$B \cos \theta = \frac{0.9\lambda}{d} + 4\eta \sin \theta \quad (1)$$

where B is peak width at half maximum intensity θ is the Bragg angle (radian), d is the crystallite size (nm), λ is the wavelength (1.54 Å) of the X-ray. η is the macro-strain.[44]

2.1.2. Electron microscopy. Particle size, morphology, and chemical composition of the milled powders were confirmed using scanning electron microscope (ZEISS SUPRATM 50 VP) equipped with energy-dispersive X-ray spectroscopy (EDS). Powder samples were dispersed in ethanol and sonicated for 180 s to avoid localized clustering of powder particles. SEM images were captured by transferring the sonicated powders on a glass plate. Further crystallite size and degree of crystallinity of the milled powders were examined using transmission electron microscopy (TECNAI, FEI, USA) operated with an accelerating voltage of 300 kV.

2.1.3. Thermal analysis. The thermal stability of the milled powders was studied using a Simultaneous Thermal Analyzer (PerkinElmer, STA 6000). Activation energy was calculated using Kissinger analysis. Experiments were performed at various heating rates *viz.*, 2, 4, 6, 8 & 10 °C min^{-1} in the temperature range of 40–400 °C. High pure argon (99.99%) gas was purged continuously at 60 ml min^{-1} during the analysis.

2.2. Electro-chemical behaviour of $Mg_{0.8-x}Ti_{0.2}$ (X = Sc, Zr, and Nb)

2.2.1. Working electrode preparation. The working electrode (pellet) was prepared by cold pressing the powder mixture containing the alloy and nickel powder in the weight ratio of 1 : 3 at 20 MPa. The dimension of the pellet after compaction was found to be ~10 mm dia. and 1 mm in thickness.

2.2.2. Electro-chemical characteristics. The Electrochemical behaviour of the developed electrode materials was studied using a Potentiostat/Galvanostat (SP150, Biologic)

setup. Studies were carried out at room temperature in a 6 M KOH electrolyte solution. A three electrode cell setup consisting of a working electrode (prepared electrode material), NiOOH/$Ni(OH)_2$ as a counter electrode, and Hg/HgO as a reference electrode were used for analysis. Cyclic voltammetry (CV) measurements were performed on the developed electrode materials with a scanning rate of 1 mV s^{-1} and in the potential range of −0.4 to −1.1 V. The charge–discharge studies on Sc, Zr and Nb substituted Mg–Ti alloys were carried out between the potential limits of −0.4 and −1.1 V at a current density of 20 mA g^{-1}. Electrochemical Impedance Spectroscopy (EIS) measurements were carried out at the varying frequency range from 100 mHz to 1 MHz with a sinusoidal amplitude of 10 mV.

3. Results and discussion

3.1. Structural and morphological characterization

The XRD pattern of the pure Mg–Ti powder and ball-milled intermetallic alloy is presented in Fig. 1. As observed, the unmilled Mg–Ti is shown in Fig. 1(a). It consists of major peaks of Mg especially (002), (010) planes with maximum intensity for (011) plane, and a few more are (012), (110), (013) and (112). Apart from those two minor peaks observed for Ti only at 2θ = 38.22° and 40.12° corresponding to (002) and (011). Comparing the unmilled and milled X-ray diffraction pattern, pristine peaks of Mg and Ti have disappeared during milling, followed by a strong shift in the inter-planar spacing. As the pure Mg–Ti powders were milled for 30 hours, the broad peak appeared only at two positions of 2θ at 42.7° and 61.9°, confirming the formation of a face-cantered cubic Mg–Ti intermetallic alloy. The inter-planar spacing value (major peak of Mg) before and after milling is found to be 0.24 nm and 0.21 nm for Mg–Ti alloy respectively. The inter-planar shift towards the lower diffraction angle points out the intense lattice distortion introduced in Mg and Ti particles during milling. Both, the absence of Mg and Ti peaks followed by the shift in major peak (Fig. 1 b–e) confirm the formation of Mg–Ti solid solution.[45,46] Again, the substitution of Zr in to Mg–Ti alloys shifts the lower diffraction angle of

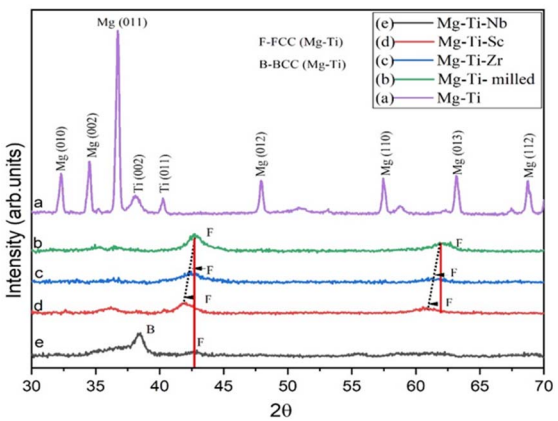

Fig. 1 Powder diffraction patterns of 30 h milled (a) pristine $Mg_{0.8}Ti_{0.2}$ (b) $Mg_{0.8}Ti_{0.2}$ (c) $Mg_{0.6}Ti_{0.2}Sc_{0.2}$ (d) $Mg_{0.6}Ti_{0.2}Zr_{0.2}$ (e) $Mg_{0.6}Ti_{0.2}Nb_{0.2}$ alloy powders.

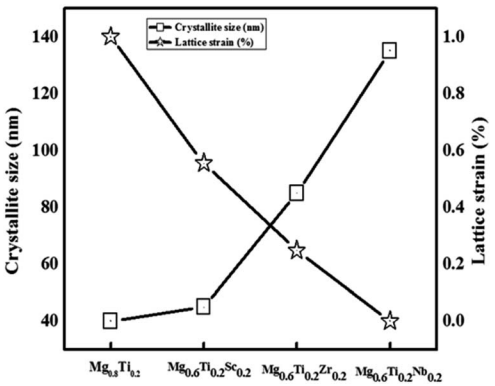

Fig. 2 Effect of Sc, Zr, and Nb substitution for Mg–Ti on the crystallite size and lattice strain of milled powders.

42.3°, increasing the d spacing value to 0.21 nm and the other peak at 61.95° corresponding to the d spacing value of 0.15 nm. However, the structure of alloys remains FCC, which is indicated in the graph as "F" for all samples. When substituting Sc for Mg–Ti alloys, main peak shift towards a lower diffraction angle of 41.9° and 60.69° concerning (Mg–Ti)–Zr intermetallic alloy, but still reminds to be FCC structure. A special case was observed when Nb was substituted for Mg–Ti intermetallic alloy, with two peaks observed at 38.42° and 42.7° corresponding to d spacing values of 0.23 and 0.21 nm respectively, among them BCC structure is dominated FCC.[47]

The effect of Sc, Zr, and Nb substitution on the crystallite size and lattice strain of Mg–Ti milled powders is shown in Fig. 2. The crystallite size of $Mg_{0.8}Ti_{0.2}$ powders milled for 30 h is around 40 nm. Upon substituting Sc, Zr, and Nb for Mg, the powder particles encountered relatively lower lattice strain resulting in larger crystallite size. It can be concluded that substituting Sc, Zr, and Nb provides a cushioning effect for Mg–Ti powder particles during milling. This cushioning effect must have sustained fracturing and enhanced cold welding, leading to larger crystallite in the milled powders. Peak broadening of $Mg_{0.8}Ti_{0.2}$, $Mg_{0.6}Ti_{0.2}Sc_{0.2}$, $Mg_{0.6}Ti_{0.2}Zr_{0.2}$ and $Mg_{0.6}Ti_{0.2}Nb_{0.2}$ powder patterns (Fig. 1) acknowledges the lattice strain and crystallite size results.

3.2. Surface morphology and elemental analysis

SEM image of ball milled $Mg_{0.8}Ti_{0.2}$, $Mg_{0.6}Ti_{0.2}Sc_{0.2}$, $Mg_{0.6}Ti_{0.2}Zr_{0.2}$, and $Mg_{0.6}Ti_{0.2}Nb_{0.2}$ alloy powders are shown in the Fig. 3. $Mg_{0.8}Ti_{0.2}$ alloy powders show homogeneously distributed equiaxed particles. Substituting Sc, Zr, and Nb for Mg–Ti leads to gradual agglomeration of powder particles, resulting in spongy morphology. The substitution of these metals causes cushioning effect during the milling. This cushioning effect must have suppressed fracturing and enhanced the cold welding of powder particles, resulting in a larger particle size of the milled powders. Nevertheless, there is no evidence of the formation of any defined structure, showing a porous structure with an amorphous structure for all milled samples, which will help during hydrogen storage. The EDS analysis confirms the formation of oxides for all samples along with mixed intermetallic powders.

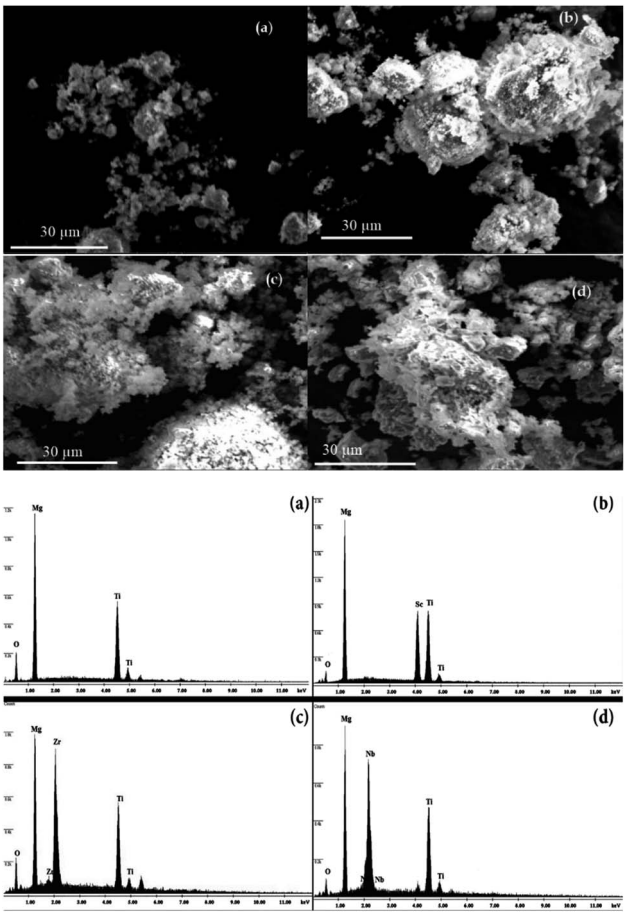

Fig. 3 SEM and their corresponding EDS images of ball-milled (a) $Mg_{0.8}Ti_{0.2}$ (b) $Mg_{0.6}Ti_{0.2}Sc_{0.2}$ (c) $Mg_{0.6}Ti_{0.2}Zr_{0.2}$ and (d) $Mg_{0.6}Ti_{0.2}Nb_{0.2}$ alloy powders.

3.3. Transmission electron microscope

Fig. 4 shows TEM micrographs and their corresponding SAED (an inset) of ball-milled $Mg_{0.8}Ti_{0.2}$, $Mg_{0.6}Ti_{0.2}Sc_{0.2}$, $Mg_{0.6}Ti_{0.2}Zr_{0.2}$, and $Mg_{0.6}Ti_{0.2}Nb_{0.2}$ alloy powders. All the milled powders exhibit inhomogeneous crystallite size distribution and this goes in congruence with SEM results. SAED pattern of $Mg_{0.8}Ti_{0.2}$ alloy powders exhibits nanocrystalline nature owing to its polycrystalline ring pattern. While the SAED pattern of $Mg_{0.8}Ti_{0.2}$, $Mg_{0.6}Ti_{0.2}Sc_{0.2}$, and $Mg_{0.6}Ti_{0.2}Zr_{0.2}$ alloy powders exhibit FCC structure and a partial diffused ring pattern, confirming partly amorphous nature as a consequence of 30 hours of ball milling. The Nb substituted Mg–Ti intermetallic alloy shows the presence of BCC structure with visible FCC too, however, the background is again amorphous.

3.4. Thermal behavior of milled powder

Crystallization kinetics of ball-milled $Mg_{0.8}Ti_{0.2}$, $Mg_{0.6}Ti_{0.2}Sc_{0.2}$, $Mg_{0.6}Ti_{0.2}Zr_{0.2}$, and $Mg_{0.6}Ti_{0.2}Nb_{0.2}$ alloy powders are given in Fig. 5. The crystallization temperature corresponding to the first and second crystallization steps are shown in the Fig. 6 and Table 1. Exothermic peaks are observed in the temperature range of ~260–350 °C and ~550–560 °C. Two exothermic peaks can be seen from the DTA profiles of $Mg_{0.8}Ti_{0.2}$ and

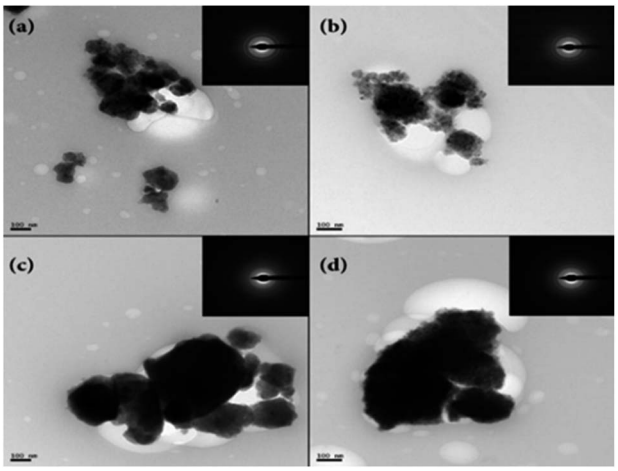

Fig. 4 TEM images and their corresponding SAED pattern of ball-milled (a) $Mg_{0.8}Ti_{0.2}$ (b) $Mg_{0.6}Ti_{0.2}Sc_{0.2}$ (c) $Mg_{0.6}Ti_{0.2}Zr_{0.2}$ and (d) $Mg_{0.6}Ti_{0.2}Nb_{0.2}$ alloy powders.

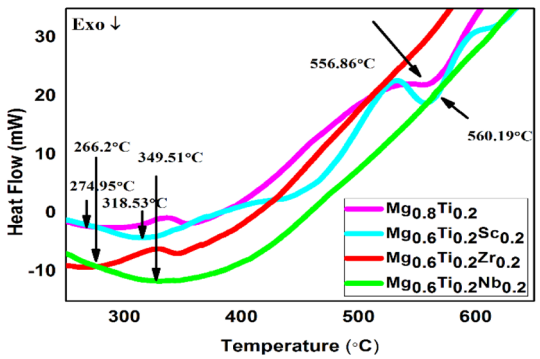

Fig. 5 Crystallization kinetics of ball milled $Mg_{0.8}Ti_{0.2}$, $Mg_{0.6}Ti_{0.2}Sc_{0.2}$, $Mg_{0.6}Ti_{0.2}Zr_{0.2}$ and $Mg_{0.6}Ti_{0.2}Nb_{0.2}$ alloy powders.

$Mg_{0.6}Ti_{0.2}Sc_{0.2}$ alloy powders. Ball milling of $Mg_{0.8}Ti_{0.2}$ powder must have resulted in a supersaturated solid solution of Ti in Mg. Here, Ti is anticipated to be in a supersaturated state in Mg owing to the limited solid solubility of Mg in Ti (<2.9 at%).[48] As a result, the two exothermic peaks at 274 °C and 556.86 °C must possibly indicate the recrystallization of the temperature of Mg(Ti).[49] Exothermic peak broadening increases after substitution of Nb and Zr in $Mg_{0.8}Ti_{0.2}$. Possible reasons for the exothermic peak broadening could be MA and resulting lattice strain induced. Thus, the calculated lattice strain from XRD analysis goes in congruence with DTA analysis.

To estimate the minimum energy required for initiating a chemical reaction, a Kissinger analysis was performed. Apparent activation energy is calculated using the Kissinger equation.[42,50]

$$\frac{d\left[\ln\left(\beta/T^2m\right)\right]}{d\left(1/T^2m\right)} = -E_a/R \quad (2)$$

where β is the heating rate in °C min^{-1}, T_m is the temperature at which the dehydriding rate was the highest in °C, E_a = activation energy in kJ mol^{-1} and R is gas constant. The Kissinger plot

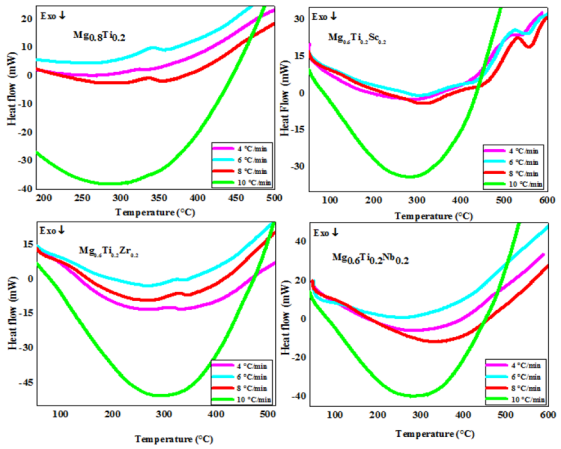

Fig. 6 DTA curves of ball milled (a) $Mg_{0.8}Ti_{0.2}$ (b) $Mg_{0.6}Ti_{0.2}Sc_{0.2}$ (c) $Mg_{0.6}Ti_{0.2}Zr_{0.2}$ and (d) $Mg_{0.6}Ti_{0.2}Nb_{0.2}$ alloy powders at different heating rates.

Table 1 The shift in the peak temperature of milled powders under different heating rate

Sample	Heating rate (°C min^{-1})	T_p (°C)
$Mg_{0.8}Ti_{0.2}$	4	304.43
	6	567.40
	8	610.39
	10	—
$Mg_{0.6}Ti_{0.2}Sc_{0.2}$	4	259.48
	6	321.17
	8	636.82
	10	700.51
$Mg_{0.6}Ti_{0.2}Zr_{0.2}$	4	545.06
	6	555.57
	8	561.47
	10	707.93
$Mg_{0.6}Ti_{0.2}Nb_{0.2}$	4	352.14
	6	—
	8	661.98
	10	—

is obtained by plotting $\ln(\beta/T_m^2)$ *versus* (T_m^{-1}).[51,52] Fig. 7 shows the Kissinger plot of ball-milled $Mg_{0.8}Ti_{0.2}$, $Mg_{0.6}Ti_{0.2}Sc_{0.2}$, $Mg_{0.6}Ti_{0.2}Zr_{0.2}$, and $Mg_{0.6}Ti_{0.2}Nb_{0.2}$ alloy powders. The minimum activation energy of 188 kJ mol^{-1} is observed in $Mg_{0.8}Ti_{0.2}$ alloy powder. Possible reasons for the lower activation energy of $Mg_{0.8}Ti_{0.2}$ alloy powder could be: severe lattice distortion (strain) experienced during milling, smaller crystallite size, and particle size distribution. Upon substituting Sc, Zr, and Nb for Mg, the activation energy increases. According to the collision theory, the lower the activation energy faster will be the chemical kinetics among the reacting species. Thus, $Mg_{0.8}Ti_{0.2}$ may quickly involve in a chemical reaction than $Mg_{0.6}Ti_{0.2}Sc_{0.2}$, $Mg_{0.6}Ti_{0.2}Zr_{0.2}$, and $Mg_{0.6}Ti_{0.2}Nb_{0.2}$ alloy powders. Owing to higher lattice strain, short crystalline order and large particle size of $Mg_{0.6}Ti_{0.2}Sc_{0.2}$, $Mg_{0.6}Ti_{0.2}Zr_{0.2}$, and $Mg_{0.6}Ti_{0.2}Nb_{0.2}$ alloy powders, the activation energy certainly increases. When the activation energy of the reacting species is larger, the larger will

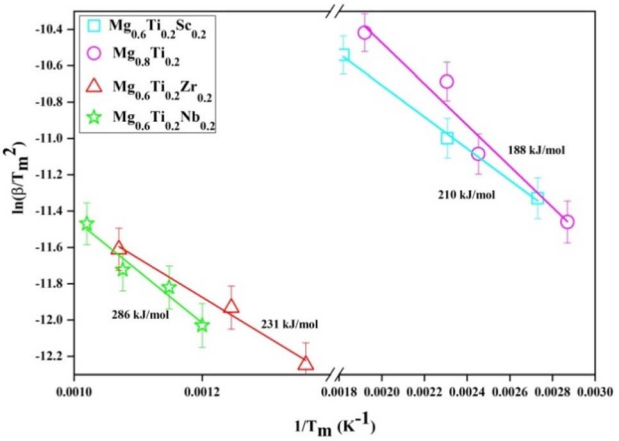

Fig. 7 Kissinger analysis of ball milled $Mg_{0.8}Ti_{0.2}$, $Mg_{0.6}Ti_{0.2}Sc_{0.2}$, $Mg_{0.6}Ti_{0.2}Zr_{0.2}$ and $Mg_{0.6}Ti_{0.2}Nb_{0.2}$ alloy powders.

be the barrier to initiating a chemical reaction. Thus, XRD and SEM observations go in congruence with the Kissinger analysis.

3.5. Electrochemical characteristics

Typical cyclic voltammetry of $Mg_{0.8}Ti_{0.2}$, $Mg_{0.6}Ti_{0.2}$ $Sc_{0.2}$, $Mg_{0.6}Ti_{0.2}$ $Zr_{0.2}$, and $Mg_{0.6}Ti_{0.2}$ $Nb_{0.2}$ alloys are shown in Fig. 8. The cathodic and anodic peaks are due to the oxidation/reduction behavior of absorbed/desorbed hydrogen atoms at the surface. A drenched cathodic peak is observed at −0.83 V for $Mg_{0.8}Ti_{0.2}$. This plateau is probably associated with the absorption of a hydrogen atom on the electrode surface and explained using following reaction

$$H_2O + e^- + M \leftrightarrow MH_{ads} + OH^- \quad (3)$$

The peak at around −1.1 V in the cathodic branch has been seen as a tail to the left in the Fig. 8. It is associated with hydrogen evolution at the electrode surface according to

$$2H_2O + 2e^- \leftrightarrow H_2(g) + 2OH^- \quad (4)$$

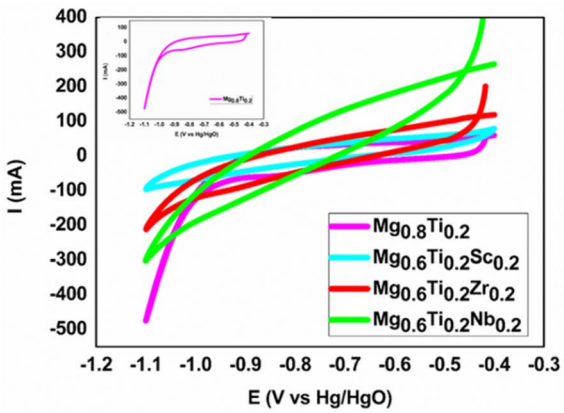

Fig. 8 Cyclic voltammetry curve of $Mg_{0.8}Ti_{0.2}$, $Mg_{0.6}Ti_{0.2}$ $Sc_{0.2}$, $Mg_{0.6}Ti_{0.2}$ $Zr_{0.2}$ and $Mg_{0.6}Ti_{0.2}$ $Nb_{0.2}$ alloys.

Gas evolution is observed at the electrode in the cathodic branch, which indicates that the reaction stated above occurs. The weak anodic peak is observed at −0.71 V. This peak is associated with the desorption of hydrogen atoms from the electrode surface according to

$$MH_{ads} + OH^- \leftrightarrow M + H_2O + e^- \quad (5)$$

Upon Sc substitution in Mg, an imperceptible cathodic and anodic peak is obtained in the range between −0.5 V and −0.6 V. E_a: anodic potential; E_c: cathodic potential; $\Delta E_{a,c}$: the difference between the anodic and cathodic potential ($E_a - E_c$). $\Delta E_{a,c}$ is taken as an estimate of the reversibility of the redox reaction. It can be seen that $\Delta E_{a,c}$ value become smaller with the addition of Sc (Table 2). This suggests that the electro–catalytic activity of the Sc-based Mg–Ti electrode has higher reversibility than the MgTi electrode. It means, the charge/discharge process appears to occur more reversible. Zr and Nb have limited positive effects on hydrogen absorption and desorption. Cathodic and anodic peaks are not observed in Zr and Nb substituted for Mg–Ti alloy. This alloy decreases the hydrogen redox behavior due to the dense oxide layer on the surface of the alloy electrode.[42,43] This prevents the further diffusion of the hydrogen atom.

Nyquist plots of $Mg_{0.8}Ti_{0.2}$, $Mg_{0.6}Ti_{0.2}Sc_{0.2}$, $Mg_{0.6}Ti_{0.2}Zr_{0.2}$, and $Mg_{0.6}Ti_{0.2}Nb_{0.2}$ alloys are presented in the Fig. 9. The electrochemical impedance spectrum consists of two semicircles followed by a short straight line at the low-frequency region, where R_s is the electrolyte/solution resistance. A smaller semicircle in the high-frequency region corresponds to the contact resistance between the current collector and pellet of the electrode material. The semicircle in the medium frequency region is related to charge transfer resistance (R_{ct}) and double-layer capacitance (C_{dl}) of the electrode material. The slope line corresponding to diffusion in the low-frequency region is described as Warburg impedance (W), which is the characteristic behaviors of hydrogen absorption and desorption. From the Nyquist plot, $Mg_{0.8}Ti_{0.2}$ exhibits a depressed semicircle and lower R_{ct} values compared to other alloys, as shown in Table 3.

Table 2 The cathodic and anodic potential of $Mg_{0.8}Ti_{0.2}$ and $Mg_{0.6}Ti_{0.2}$ $Sc_{0.2}$ alloy electrodes

Sample	E_a (V)	E_c (V)	$\Delta E_{a,c}$ (V)
$Mg_{0.8}Ti_{0.2}$	−0.83	−0.71	−0.12
$Mg_{0.6}Ti_{0.2}Sc_{0.2}$	−0.5	−0.6	−0.1

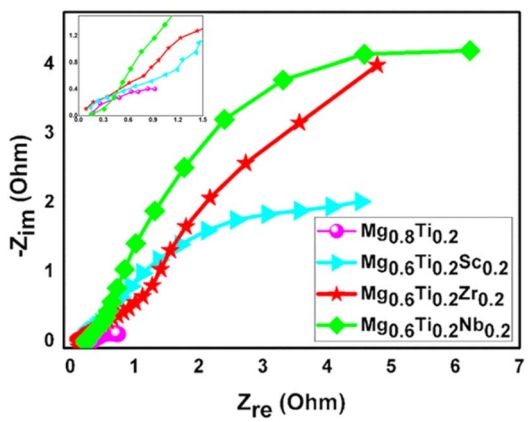

Fig. 9 Nyquist plots of $Mg_{0.8}Ti_{0.2}$, $Mg_{0.6}Ti_{0.2}Sc_{0.2}$, $Mg_{0.6}Ti_{0.2}Zr_{0.2}$ and $Mg_{0.6}Ti_{0.2}Nb_{0.2}$ alloys.

Table 3 EIS parameters of $Mg_{0.8}Ti_{0.2}$, $Mg_{0.6}Ti_{0.2}Sc_{0.2}$, $Mg_{0.6}Ti_{0.2}Zr_{0.2}$ and $Mg_{0.6}Ti_{0.2}Nb_{0.2}$ electrode materials

Alloy	R_s (Ω)	R_{ct} (Ω)	C_{dl} (μF)	D (cm^2 s^{-1})
$Mg_{0.8}Ti_{0.2}$	0.17	0.94	13.11	9.40×10^{-9}
$Mg_{0.6}Ti_{0.2}Sc_{0.2}$	0.20	4.34	12.81	2.23×10^{-10}
$Mg_{0.6}Ti_{0.2}Zr_{0.2}$	0.23	4.65	9.19	9.33×10^{-11}
$Mg_{0.6}Ti_{0.2}Nb_{0.2}$	0.24	5.98	7.58	8.08×10^{-11}

Diffusion coefficient estimated using the following formula

$$D = \frac{R^2T^2}{2A^2n^4c^2\sigma^2} \quad (6)$$

where R is the gas constant, T is the absolute temperature, n is the number of electrons involved in the reaction, A is the surface area, F is the Faraday's constant, c is the concentration and D is the diffusion coefficient (cm^2 s^{-1}) and σ is the coefficient of Warburg impedance which can be obtained from the intersection of the straight line on the real axis. It is equal to ($R_s + R_{ct} - 2\sigma^2C_{dl}$).

Ti substitution for Mg leads to a porous oxide layer $Mg(OH)_2$ formation on the surface of electrode material. This oxide layer increases the specific surface area and enhances the kinetics of the charge transfer reaction. The charge transfer resistance of $Mg_{0.6}Ti_{0.2}Sc_{0.2}$ is lower than $Mg_{0.6}Ti_{0.2}Zr_{0.2}$ and $Mg_{0.6}Ti_{0.2}Nb_{0.2}$ alloy but higher than $Mg_{0.8}Ti_{0.2}$ electrode materials. Sc forms a thin porous oxide layer over Mg–Ti and this oxide layer partially covers the electrode surface leaving a substantial amount of MgTi atoms open for ionic transportation in an electrolyte solution. While the substitution of Zr and Nb in Mg has resulted a higher charge transfer resistance value owing to the formation of a stable oxide/hydroxide layer on the electrode surface.[42,53–55] This hydroxide layer completely covers the electrode surface, thereby limiting the electrochemical kinetics of the electrode material. Consequently, the double layer capacitance (C_{dl}) and diffusion coefficient of electrode material decrease. Thus, ascribed discussion from impedance analysis is quite consistent with DTA analysis.

The discharge curves of $Mg_{0.8}Ti_{0.2}$, $Mg_{0.6}Ti_{0.2}Sc_{0.2}$, $Mg_{0.6}Ti_{0.2}Zr_{0.2}$, and $Mg_{0.6}Ti_{0.2}Nb_{0.2}$ electrodes are shown in the Fig. 10. The initial discharge capacities of $Mg_{0.8}Ti_{0.2}$, $Mg_{0.6}Ti_{0.2}Sc_{0.2}$, $Mg_{0.6}Ti_{0.2}Zr_{0.2}$, and $Mg_{0.6}Ti_{0.2}Nb_{0.2}$ electrode materials are found to be 535, 514, 333 and 202 mA h g^{-1} respectively. The discharge behavior of Ti and Sc substituted electrode materials is significantly better than that of the Zr and Nb substituted electrode materials. Both, the smaller crystal size and lower activation energy of $Mg_{0.8}Ti_{0.2}$ and $Mg_{0.6}Ti_{0.2}Sc_{0.2}$

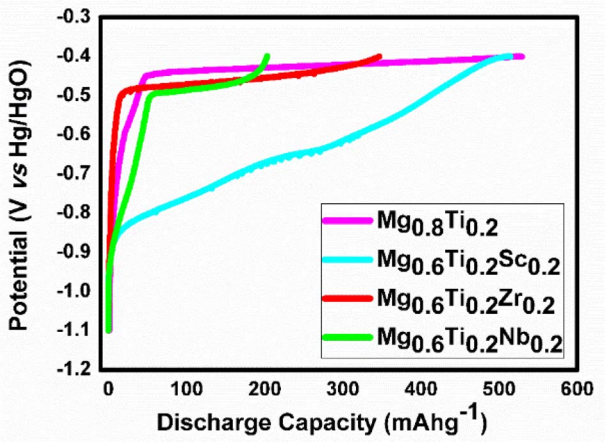

Fig. 10 Discharge curve of $Mg_{0.8}Ti_{0.2}$, $Mg_{0.6}Ti_{0.2}Sc_{0.2}$, $Mg_{0.6}Ti_{0.2}Zr_{0.2}$ and $Mg_{0.6}Ti_{0.2}Nb_{0.2}$ electrode materials.

must have resulted in the superior discharge kinetics. Discharge capacity *vs.* cycle number of $Mg_{0.8}Ti_{0.2}$, $Mg_{0.6}Ti_{0.2}Sc_{0.2}$, $Mg_{0.6}Ti_{0.2}Zr_{0.2}$, and $Mg_{0.6}Ti_{0.2}Nb_{0.2}$ electrodes is shown in the Fig. 11. All the electrode materials reveal higher discharge capacity during their first cycle and then gradually decrease with increasing cycle number.

The capacity retentions of $Mg_{0.8}Ti_{0.2}$, $Mg_{0.6}Ti_{0.2}Sc_{0.2}$, $Mg_{0.6}Ti_{0.2}Zr_{0.2}$, and $Mg_{0.6}Ti_{0.2}Nb_{0.2}$ electrode materials are shown in the Fig. 12. The capacity retention is used to represent the cycling stability of the developed electrode materials. It can be calculated from the following equation,

$$S_n(\%) = \frac{C_n}{C_{max}} \times 100\% \quad (7)$$

The initial discharge capacity of a Ti substituted Mg-based electrode is very high but the cycling property is relatively less than the Sc substituted electrode materials. Sc substitution in Mg helps to transform the compact Ti oxide film into a porous oxide layer which leads to better capacity retention than other

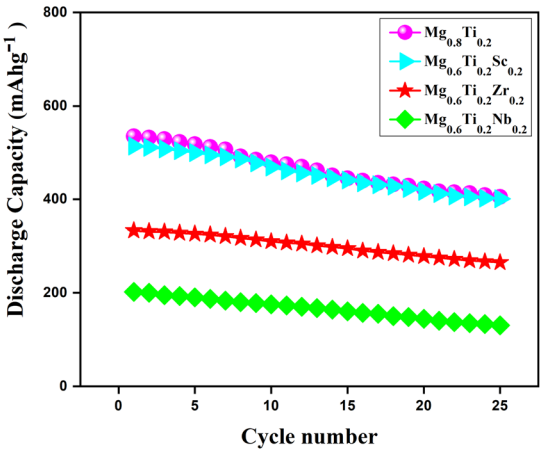

Fig. 11 Discharge capacity *vs.* cycle number of $Mg_{0.8}Ti_{0.2}$,$Mg_{0.6}Ti_{0.2}Sc_{0.2}$, $Mg_{0.6}Ti_{0.2}Zr_{0.2}$ and $Mg_{0.6}Ti_{0.2}Nb_{0.2}$ electrode materials.

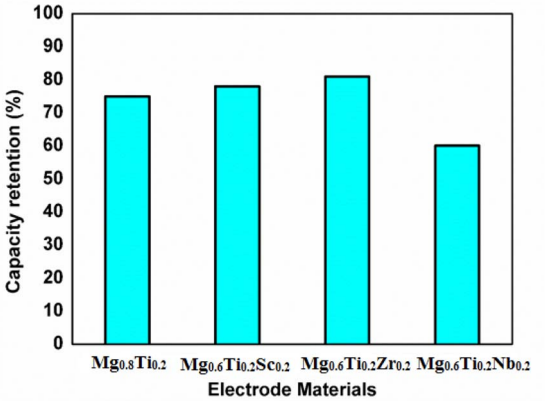

Fig. 12 Capacity retentions of $Mg_{0.8}Ti_{0.2}$, $Mg_{0.6}Ti_{0.2}Sc_{0.2}$, $Mg_{0.6}Ti_{0.2}Zr_{0.2}$ and $Mg_{0.6}Ti_{0.2}Nb_{0.2}$ alloys.

electrode materials. Zr substitution in Mg improves the cyclic life of the MgTi electrode significantly owing to the formation of a stable oxide layer on the electrode surface. Nb substitution for Mg results in a dense oxide layer formation on the electrode surface owing to the difference in their electronegativity values. This dense oxide layer limits the mobility of hydrogen ions leading to inferior discharge kinetics of the electrode material. Since the activation energy is also high for Nb substituted alloy, so it leads to poor discharge capacity.

4. Conclusion

Mechanically alloyed Mg–Ti intermetallic compound shows the formation of FCC structure even after milled for 30 hours. Adding 0.2 wt% of transition metals such as Sc, and Zr do not alter the FCC structure, however, the peak shift towards the lower diffraction angle confirms the increases in the *d* spacing values. A special case was observed when adding Nb, which forms a BCC structure, nevertheless, small broad peak was observed for FCC too. SEM and TEM analysis confirm the presence of porous and spongy structured samples. EDS analysis confirms the presence of all the Mg–Ti composition with Sc, Zr, and Nb along with a small amount of oxygen content for all samples. SAED and XRD analysis confirm the presence amorphous background for all transition metals (Sc, Zr and Nb) substituted samples and a crystalline phase except for the Mg–Ti alloy. Kissinger analysis confirms that $Mg_{0.8}Ti_{0.2}$ alloy powder possesses relatively higher chemical kinetics than Sc, Zr and Nb substituted Mg–Ti alloy powders, so it has maximum hydrogen storage capacity compared to other alloys. Nanocrystalline $Mg_{0.8}Ti_{0.2}$ alloy shows the maximum electrochemical discharge capacity of 535 mA h g^{-1} at 20 mA g^{-1}. This is attributed to homogenous distribution and the smaller mean size of the alloy particle, which is confirmed through TEM observation. The Sc substituted alloy shown amorphous structure and has delivered slightly lower discharge capacity and higher capacity retention as compared to $Mg_{0.8}Ti_{0.2}$ due to its porous oxide layer, resulting in favorable hydrogen absorption/desorption kinetics. Zr substitution in Mg improves the cyclic life of the MgTi electrode

significantly owing to the formation of a stable oxide layer on the electrode surface. The substitution of Nb enhances the higher charge transfer resistance and shows poor discharge capacity and capacity retention.

Author contributions

K. S. Nivedhitha: conceptualization, data curation; formal analysisfunding-acquisition **https://credit.niso.org/contributor-roles/funding-acquisition/**; investigation; methodology; resources; supervision; validation: visualization: writing – original draft: writing – review & editing. R. Venkatesh: conceptualization, formal analysisfunding-acquisition **https://credit.niso.org/contributor-roles/funding-acquisition/**; investigation; methodology; validation: visualization: writing – original draft: writing – review & editing. N. R. Banapurmath: investigation; methodology; validation: visualization: writing – original draft: writing – review & editing. T. M. Yunus Khan: validation; writing – review & editing. Chandramouli Vadlamudi: validation; writing – review & editing. Sanjay Krishnappa: validation; writing – review & editing. Sultan Ashehery: validation; writing – review & editing.

Conflicts of interest

There is no conflict among authors.

Acknowledgements

The authors gratefully acknowledge the facilities support from Department of Metallurgical and Materials Engineering, National Institute of Technology, Tiruchirappalli, Tamil Nadu, India and Deanship of Scientific Research at King Khalid University for funding this work through research groups program under grant number (R.G.P 2/318/44). The authors also acknowledge KLE Technological University, for the continuous support for this research work.

Notes and references

1 W. Grochala and P. P. Edwards, *Chem. Rev.*, 2004, **104**, 1283–1316.
2 S. I. Orimo, Y. Nakamori, J. R. Eliseo, A. Züttel and C. M. Jensen, *Chem. Rev.*, 2007, **107**, 4111–4132.
3 D. B. Ravnsbæk, Y. Filinchuk, R. Cerný and T. R. Jensen, *Z. Kristallogr. Cryst. Mater.*, 2010, **225**, 557–569.
4 L. H. Rude, T. K. Nielsen, D. B. Ravnsbaek, U. Boesenberg, M. B. Ley, B. Richter, L. M. Arnbjerg, M. Dornheim, Y. Filinchuk and F. Besenbacher, *Phys. Status Solidi A*, 2011, **208**, 1754–1773.
5 G. Principi, F. Agresti, A. Maddalena and S. Lo Russo, *Energy*, 2009, **34**, 2087–2091.
6 K. Aoki, A. Memezawa and T. Masumoto, *J. Mater. Res.*, 1994, **9**, 39–46.
7 H. Zhang and E. H. Kisi, *J. Phys.: Condens. Matter*, 1997, **9**, L185–L190.
8 Z.-H. Cheng, G. R. MacKay, D. A. Small and R. A. Dunlap, *J. Phys. D: Appl. Phys.*, 1999, **32**, 1934–1937.
9 J. L. Bobet, C. Even, Y. Nakamura, E. Akiba and B. Darriet, *J. Alloys Compd.*, 2000, **298**, 279–284.
10 S.-I. Orimo and F. K. A. Günter Majer, *Phys. Rev. B: Condens. Matter Mater. Phys.*, 2001, **63**, 094307.
11 J. Chen, H. T. Takeshita, D. Chartouni, N. Kuriyama and T. Sakai, *J. Mater. Sci.*, 2001, **36**, 5829–5834.
12 F. C. Gennari, F. J. Castro and J. J. Andrade Gamboa, *J. Alloys Compd.*, 2002, **339**, 261–267.
13 M. Herrich, N. Ismail, J. Lyubina, A. Handstein, A. Pratt and O. Gutfleisch, *Mater. Sci. Eng., B*, 2004, **108**, 28–32.
14 L. A. Baum, M. Meyer and L. Mendoza-Zélis, *Int. J. Hydrogen Energy*, 2008, **33**, 3442–3446.
15 S. Deledda and B. C. Hauback, *Nanotechnology*, 2009, **20**, 204010.
16 C. Rongeat, V. D'Anna, H. Hagemann, A. Borgschulte, A. Züttel, L. Schultz and O. Gutfleisch, *J. Alloys Compd.*, 2010, **493**, 281–287.
17 T. Ichikawa, S. Isobe, N. Hanada and H. Fujii, *J. Alloys Compd.*, 2004, **365**, 271–276.
18 C. B. Minella, C. Rongeat, R. Domènech-Ferrer, I. Lindemann, L. Dunsch, N. Sorbie, D. H. Gregory and O. Gutfleisch, *Faraday Discuss.*, 2011, **151**, 253–262.
19 P. Muthu and K. Sinnaeruvadi, *J. Alloys Compd.*, 2019, **793**, 155–169.
20 P. Muthu and K. Sinnaeruvadi, *Mater. Chem. Phys.*, 2021, **274**, 125129.
21 X. D. Bai, D. Zhong, G. Y. Zhang, X. C. Ma, S. Liu, E. G. Wang, Y. Chen and D. T. Shaw, *Appl. Phys. Lett.*, 2001, **79**, 1552–1554.
22 P. Vermeulen, H. J. Wondergem, P. C. J. Graat, D. M. Borsa, H. Schreuders, B. Dam, R. Griessen and P. H. L. Notten, *J. Mater. Chem.*, 2008, **18**, 3680–3687.
23 P. H. L. Notten, M. Ouwerkerk, H. van Hal, D. Beelen, W. Keur, J. Zhou and H. Feil, *J. Power Sources*, 2004, **129**, 45–54.
24 R. Venkatesh, N. R. Banapurmath, S. Modagi, S. A. Hallod and A. S. Shetter, *Mater. Today: Proc.*, 2020, **27**, 59–61.
25 R. Venkatesh, N. R. Banapurmath, A. Palrecha and K. Ramesh, *IOP Conf. Ser.: Mater. Sci. Eng.*, 2020, **872**, 012189.
26 R. Venkatesh, P. Murahari, N. R. Banapurmath and K. Ramesh, *Nano-Struct. Nano-Objects*, 2022, **30**, 100878.
27 V. Ramasamy, P. Munga and R. Karuppannan, *Diamond Relat. Mater.*, 2021, **111**, 108172.
28 P. Munga, R. Venkatesh, N. Naresh, A. Sankhla, E. S. R. Gopal and K. Ramesh, *J. Non-Cryst. Solids*, 2016, **447**, 178–182.
29 L. Lü and M. O. Lai, The Mechanical Alloying Process, in *Mechanical Alloying*, Springer, Boston, MA, 1998, pp. 23–67.
30 H. Chu, Y. Zhang, L. Sun, S. Qiu, F. Xu, H. Yuan, Q. Wang and D. Chuang, *Int. J. Hydrogen Energy*, 2007, **32**, 3363–3369.
31 W. P. Kalisvaart, R. A. H. Niessen and P. H. L. Notten, *J. Alloys Compd.*, 2006, **417**, 280–291.
32 R. A. H. Niessen and P. H. L. Notten, *J. Alloys Compd.*, 2005, **404–406**, 457–460.

33 R. A. H. Niessen and P. H. L. Notten, *Electrochem. Solid-State Lett.*, 2005, **8**, A534.
34 R. A. H. Niessen, P. Vermeulen and P. H. L. Notten, *Electrochim. Acta*, 2005, **51**, 2427–2436.
35 W. P. Kalisvaart, M. Latroche, F. Cuevas and P. H. L. Notten, *J. Solid State Chem.*, 2008, **181**, 1141–1148.
36 N. H. Goo, W. T. Jeong and K. S. Lee, *J. Power Sources*, 2000, **87**, 118–124.
37 Y.-h. Zhang, D.-l. Zhao, X.-y. Han, B.-w. Li, X.-p. Dong and X.-l. Wang, *Int. J. Hydrogen Energy*, 2007, **32**, 2830–2835.
38 Y.-h. Zhang, X.-y. Han, B.-w. Li, H.-p. Ren, X.-p. Dong and X.-l. Wang, *J. Alloys Compd.*, 2008, **450**, 208–214.
39 M. Anik, H. Gasan, S. Topcu, I. Akay and N. Aydinbeyli, *Int. J. Hydrogen Energy*, 2009, **34**, 2692–2700.
40 M. Anik, I. Akay and S. Topcu, *Int. J. Hydrogen Energy*, 2009, **34**, 5449–5457.
41 M. Anik, *J. Alloys Compd.*, 2009, **486**, 109–114.
42 M. Anik, I. Akay, G. Özdemir and B. Baksan, *Int. J. Hydrogen Energy*, 2009, **34**, 9765–9772.
43 N. Hanada, T. Ichikawa and H. Fujii, *J. Alloys Compd.*, 2007, **446–447**, 67–71.
44 K. S. Nivedhitha, R. Venkatesh and N. R. Banapurmath, *Phys. Scr.*, 2023, **98**, 015706.
45 D. M. J. Wilkes, P. S. Goodwin, C. M. Ward-Close, K. Bagnall and J. Steeds, *Mater. Lett.*, 1996, **27**, 47–52.
46 N. F. Albanese-Kotar and D. E. Mikkola, *Mater. Sci. Eng.*, 1987, **91**, 233–240.
47 K. Asano, H. Enoki and E. Akiba, *J. Alloys Compd.*, 2009, **480**, 558–563.
48 J. L. Murray, *Bull. Alloy Phase Diagrams*, 1986, **7**, 245–248.
49 I. Obinata, Y. Takeuchi and R. Kawanishi, *MTLLA*, 1959, 13.
50 H. E. Kissinger, *Anal. Chem.*, 1957, **29**, 1702–1706.
51 K. Yang, Z. Deng and J. Suo, *J. Power Sources*, 2012, **201**, 274–279.
52 M. Shi, Z. Chen and J. Sun, *Cem. Concr. Res.*, 1999, **29**, 1111–1115.
53 S.-M. Lee, H. Lee, J.-H. Kim, P. S. Lee and J.-Y. Lee, *J. Alloys Compd.*, 2000, **308**, 259–268.
54 V. Ayyavu and K. Sinnaeruvadi, *Mater. Express*, 2015, **5**.
55 V. Ayyavu, N. Chandrasekar and K. Sinnaeruvadi, *Part. Sci. Technol.*, 2015, **34**, 134–142.